Comparison between Ni–Rh/gadolinia doped ceria catalysts in reforming of propane for anode implementations in intermediate solid oxide fuel cells

M. Boaro [a,*], V. Modafferi [b], A. Pappacena [a], J. Llorca [c], V. Baglio [d], F. Frusteri [d], P. Frontera [b], A. Trovarelli [a,e], P.L. Antonucci [b,e]

[a] Università di Udine, Dipartimento di Scienze e Tecnologie Chimiche, via Cotonificio 108, 33100 Udine, Italy
[b] Università Mediterranea, Dipartimento Meccanica e Materiali, Feo di Vito, 89060 Reggio Calabria, Italy
[c] Institut de Tècniques Energètiques, Universitat Politècnica de Catalunya, Diagonal 647, ed. ETSEIB, 08028 Barcelona, Spain
[d] CNR-ITAE "Nicola Giordano", Salita S. Lucia 5, 98126 Messina, Italy
[e] INSTM-Consorzio Interuniversitario Nazionale per le Scienze e Tecnologie dei Materiali, via Giusti 9, 50121 Firenze, Italy

ABSTRACT

Steam and autothermal reforming of propane over Ni–Rh/GDC catalysts prepared by coprecipitation and by Pechini method were investigated in the temperature range 873–1073 K. The weight ratio for Ni, Rh and $Ce_{0.8}Gd_{0.2}O_2$ (45:5:50) and the operating temperatures were chosen in order to gain propaedeutical information on fuel reactivity under typical intermediate solid oxide fuel cell (IT-SOFC) operating conditions.

The Pechini synthesis allows to obtain catalysts with lower surface area, smaller nickel crystallites and a bimodal distribution of rhodium in comparison to the coprecipitation method. Despite the different methods of synthesis lead to catalysts with different morphological and structural properties, the activity of catalysts is quite similar.

At reaction temperature higher than 973 K, under both steam reforming (SR) and autothermal reforming (ATR), the catalysts show high propane conversion and syngas ($H_2 + CO$) productivity.

Deactivation of catalysts was observed at 873 and 973 K under SR conditions due to coke formation.

In ATR, coke formation was almost completely depressed and the catalysts resulted to be very stable even at low reaction temperature (873 K). In SR coke formation occurs with higher rate on the catalyst having higher Ni dispersion, probably since propane cracking reaction is the pre-eminent phenomenon in promoting coke formation.

© 2009 Elsevier B.V. All rights reserved.

1. Introduction

Hydrogen is nowadays considered the energy carrier of the future, to be employed as a fuel in efficient and environmentally safe energy conversion devices such as fuel cells [1,2]. The lack of an infrastructure for the production and distribution of H_2 has stimulated research in fuel processing, in particular, in the development of fuel processors for reforming widely available fuels, such as natural gas, liquefied petroleum gas, gasoline, and diesel fuel at the point of application. In parallel with the development of new fuel processors, for a short term economically competitive entrance of fuel cell technology in the market, a great attention is given to the power systems that can operate directly with logistic fuels or with H_2 rich "reformates" without further steps of purification from impurities such as CO, H_2S or NH_3.

SOFCs (solid oxide fuel cells) are, amongst the different types of fuel cells, the most versatile ones in terms of fuel flexibility [3]. They operate at temperatures high enough to allow the internal reforming of light hydrocarbons and/or their direct electro-oxidation [4–9]. In this respect, in addition to the high activity for reforming and electrochemical oxidation of fuel, the anode should be tolerant to carbon deposition formed by decomposition of hydrocarbons. Nickel is a very efficient and cost effective component of SOFC anode since it shows very high activity for the steam reforming of hydrocarbons; on the other hand, it promotes graphitic carbon formation, which leads to the anode disruption [10]. In the case of methane reforming, deactivation by coke can be limited by the control of operating temperature, by tuning the methane/steam ratio or modifying the cermet compositions [4,11,12]. Particularly efficient is the substitution of YSZ (yttria stabilized zirconia) component with ScSZ (scandia stabilized zirconia) [13,14] or ceria based oxides. Zha et al. demonstrated that at low temperatures (<923 K) methane can be directly used as a fuel into Ni-GDC (gadolinia doped ceria) SOFC anode without carbon deposition [15]. It was also reported

* Corresponding author. Tel.: +39 0432 558824; fax: +39 0432 558803.
E-mail addresses: marta.boaro@uniud.it, mboaro2000@yahoo.it (M. Boaro).

that the addition of precious or transition metals [16] contributes to depress the carbon deposition on nickel-based anode. New formulations for anode and reforming catalysts are mandatory when higher hydrocarbons than CH_4 are used as fuel [17]. Heavier hydrocarbons are preferable from the viewpoint of fuel economy, such as LPG (liquefied petroleum gas) that represents a valid alternative to the use of natural gas because easily transportable and storable on site. Propane and butane are often used as simulated LPG since they are the main constituents of this fuel. Nevertheless, their direct utilization in SOFCs requires specific strategies of reforming to limit the deactivation of the anode catalyst by deposition of carbonaceous compounds [18,19]. The deposition of carbon is generally avoided by supplying excess water to the fuel stream. For example, steam to carbon (S/C) ratio higher than 3 is needed to reduce coke in steam reforming of propane, but this will increase costs and reduce the energy efficiency. To minimize the expenses of fuel processing it has been proposed to integrate a hydrocarbon pre-reformer chamber to a low temperature SOFC [20,21].

An alternative approach proposed to limit the carbon deposition can be to use functionally graded porous anode structures with outer diffusion barriers that promote the steam reforming process by increasing the water concentration within the porous media [22].

Recently, to depress coke formation, the use of Ru as promoter of anodic oxidation of propane in SOFCs has been proposed [23,24]. $Cu\text{-}CeO_2$ was also demonstrated to be an active anode for direct electro-oxidation of butane without deactivation by coke formation [9].

Concerning the development of more effective catalyst compositions, it has been reported that the carbon resistance of the conventional Ni/Al_2O_3 improves when doped with 14% CeO_2 [25]. High surface area CeO_2 synthesized by a surfactant-assisted method provides significantly higher reforming activity and excellent resistance towards carbon deposition compared to Ni/Al_2O_3, due to the high oxygen mobility and storage capacity of ceria [26].

In spite of their elevate costs, Rh-based reforming catalysts have been also investigated for fuel processing devoted to fuel cell systems because they exhibit the highest intrinsic rate in steam reforming [27], partial oxidation and oxidative steam reforming of light hydrocarbons, particularly in a short contact time regime [28,29], associated with a high resistance to carbon formation compared to other metals [30–32]. In particular, Rh/CeO_2 has shown better reforming performance and higher resistance to coking compared to Rh/Al_2O_3, apparently due to a higher basicity and oxygen storage capacity of CeO_2 [33]. In addition, it has been reported that $Rh/Ce_{0.5}Zr_{0.5}O_2$ nano-particles prepared by flame spray synthesis yielded a very high conversion of butane to syngas without soot formation [34]. Although it has been proved that ceria-supported noble metals are suitable catalysts to avoid coke deposition during hydrocarbons reforming, their stability depends on several other factors that must be carefully considered. In fact, for these systems strong metal–support interaction phenomena may play an important role in their activation/deactivation processes, as the reforming of hydrocarbons creates a reducing atmosphere under operating conditions [35].

The role of support on the performance of Rh catalysts for the autothermal reforming of heavy hydrocarbons ($i\text{-}C_4H_{10}$) has been recently reviewed by Ferrandon and Krause [36]. The dispersion of Rh and the nature of the support were indicated as the main factors to be considered. It has been found that $Gd\text{-}CeO_2$ was a poor support for Rh, while $La\text{-}Al_2O_3$ and YSZ were found to be more adequate as carriers. Rhodium catalysts supported on GDC under steam reforming conditions (1073 K, steam to carbon ratio ∼3 and natural gas as feed) were also investigated by Hennings and Reimert [37]. These authors observed an early deactivation of freshly prepared catalysts, which showed stable performance for at least 190 h after three subsequent reduction–reaction–oxidation cycles. It has been proposed that the catalyst deactivation occurs by metal decoration under the applied reducing step.

Noble metal–Ni bimetallic catalysts have also been investigated in order to gain advantage from both the superior activity of noble metals for hydrocarbon oxidation and the catalytic properties of Ni in reforming reactions [19–21,38–41]. Concerning the partial oxidation of methane, the reported high catalytic activity of Rh/Ni catalysts was attributed to synergic effects between the two metals, where Rh allows to maintain Ni in a reduced state in the reaction environment [42].

In this work, bimetallic Ni–Rh/GDC catalysts were prepared by two different routes, i.e. coprecipitation and Pechini method. We choose the Pechini synthesis method since it ensures a very good homogeneity of the components and allows preparation of materials that generally have morphological and structural properties different from the catalysts prepared by conventional routes [43,44]. The catalysts were tested in steam and autothermal reforming of propane in the temperature range 873–1073 K. These tests are considered propaedeutical to fuel cell applications, in order to gain information on fuel reactivity at the typical IT-SOFCs operative conditions.

2. Experimental

2.1. Catalysts preparation

2.1.1. $Ce_{0.8}Gd_{0.2}O_2$ synthesis

Ceria–gadolinia carrier was prepared by hydrothermal method. Defined amounts of $Ce(NO_3)_3\cdot 6H_2O$ and $Gd(NO_3)_3\cdot 6H_2O$ were separately dissolved in water, mixed and coprecipitated with ammonium hydroxide at pH 10. The gel so obtained was hydrothermally treated at 453 K for 4 h into a teflonlined autoclave, then the autoclave was quenched and the powder was washed with distilled water and dried overnight at 358 K. The as-prepared support was then calcined in air at 573 K for 2 h.

2.1.2. Ni–Rh deposition

Ni and Rh were deposited, in weight ratio of 45:5, on GDC carrier, by coprecipitation (C1) and Pechini (C2) methods using Ni and Rh nitrates as precursors.

Coprecipitation synthesis. The GDC support was suspended for 2 h into a solution of the metal precursors, then a Na_2CO_3 (1 M) solution was added drop wise increasing the pH of solution up to 8 to precipitate the metal oxides. After stirring for almost 20 h, the precipitate was filtered, washed several times up to reach a neutral pH, dried at 353 K for 4 h and then calcined according to the following temperature program: 12 h at 673 K, from 673 to 973 K in 3 h, 5 h at 973 K.

Pechini synthesis. The Ni and Rh nitrate precursors were dissolved into distilled water, then citric acid (CA) and ethylene glycol (EG) were added into the solution as complexation/polymerization agents. The pH of the prepared solution was adjusted to 8 by adding concentrated ammonia and the temperature was raised to 323 K to favour the complexation process of metal cations, before adding the ethylene glycol. The molar ratios of CA:EG:metal ions in the solution were 1.5:6:1. After few minutes the GDC carrier was added to the solution and the final slurry was heated up to 353 K and maintained at this temperature for about 2 h to promote the polyesterification reactions. The gel so obtained was dried at 400 K for 48 h and calcined according to the temperature programme above reported.

2.2. Catalysts characterization

2.2.1. Morphological and structural properties

Structure and morphology of fresh and used catalysts were investigated by N_2 adsorption–desorption isotherms, X-ray diffractometry and electron microscopy analyses.

Nitrogen adsorption–desorption isotherms for BET surface area and BJH pore size and pore size distribution measurements were carried out with a Micrometrics TRISTAR 3000 gas analyzer at 77 K over a wide relative pressure range from 0.03 to 0.995.

X-ray powder diffraction profiles were collected with a Philips PW3040/60 X'pert PRO instrument (equipped with an X'celerator detector) operated at 40 kV and 40 mA, with Ni-filtered Cu-K$_\alpha$ radiation. Spectra were collected over the angular range $20° < 2\theta < 145°$, in a constant scan mode with steps of $0.02°$ and a counting time of 40 s. The average size of oxide particles was determined from XRD line broadening by Scherrer's equation.

High resolution transmission electron microscopy (HRTEM) investigation was carried out using a JEOL 2010F instrument equipped with a field emission gun, which allowed to achieve a point-to-point resolution of 0.19 nm and a resolution of 0.14 nm between lines, and a Philips CM12 electron microscopy provided with a high resolution camera. Samples were prepared from an ultrasonic dispersion of the catalyst in alcohol deposited on holey-carbon coated grids.

2.2.2. Temperature programmed measurements

Hydrogen chemisorption was used to determine the metal dispersion of Rh. The chemisorption measurements were carried out with a Micromeritics apparatus (AutochemII 2990) by titration of metal surface with 0.26 mL pulses of H_2 at 300 K, using a stoichiometry of 1:1 by atoms to determine the metal dispersion of Rh. The sample (50 mg) was heated under flowing air from room temperature to 773 K with a heating rate of 10 K min^{-1} and oxidized for 1 h. The chemisorption measurements have been performed after sequential reductions of the sample at 453 ond 503 K for 1 h. After every reduction step and before the chemisorption experiment, the sample was degassed under Ar flowing for 120 min at a temperature 50 K higher than that of the related reduction step.

The redox behaviour of the samples has been studied in the range 298–1273 K by temperature programmed reduction (TPR) performed in the same apparatus used for the chemisorption experiments, under flowing 5% H_2/Ar mixture at 35 STP cm^3 min^{-1}, with a heating rate of 10 K min^{-1}. Before every TPR experiment, all the samples have been oxidized in flowing air (30 STP cm^3 min^{-1}) for 1 h at 773 K, in order to remove labile adsorbates such as carbonates and hydroxides and to obtain for all catalysts the same starting conditions.

The quantitative analysis has been calculated from the peak areas after a standard calibration procedure of the TCD signal evolution.

Coke formation was evaluated by differential temperature (DTA) and thermo-gravimetric (TGA) analyses. Measurements were performed in the temperature range 298–1073 K under air flow (100 STP cm^3 min^{-1}) using a TA thermal analysis instruments (SDT-Q600) with a heating rate of 2 K min^{-1}, analyzing the products of oxidation (CO and CO_2) by a mass spectrometer (Hiden 200).

2.2.3. Catalytic tests

Catalytic measurements were carried out at atmospheric pressure, using a quartz micro-reactor (i.d. = 4 mm) by operating at high GHSV (1,600,000 h^{-1}) and reaction temperatures ranging from 873 to 1073 K. The catalyst was diluted with SiC (SiC/catalyst = 4). The reaction temperature was monitored with a thermocouple inserted into the reactor through a quartz tube. A reactor, filled with inert

Table 1
N_2 adsorption/desorption isotherm results.

Samples	SA$_{BET}$ (m^2 g^{-1})	Average pore size (Å)	Cumulative pore volume (cm^3 g^{-1})
GDC	134.1	67	0.22
Ox-C1	37.4	122	0.14
Ox-C2	10.3	60	0.021
Red-C1	27.3	94	0.082
Red-C2	11.5	73	0.030

material, held at 523 K, was used to evaporate water fed by an isocratic pump (Varian ProStar 210).

Gases, after purification by deoxo gas clean filters (Chrompack) and molecular sieve traps, were fed with calibrated mass flow controllers (Brooks 5850S). Experiments were carried out as follows:

(i) steam reforming (SR): S/C ratio = 2.5;
(ii) autothermal reforming (ATR): S/C ratio = 2.5, O/C ratio = 0.5, using O_2 as oxidizing gas.

All experiments have been carried out with a total inlet flow of 150 STP cm^3 min^{-1}. The reaction stream was analyzed on-line with a Varian micro-GC equipped with TCD detector and a three-column system (molecular sieves 5A, Porapak Q and Cpsil columns). Before analysis, water was eliminated from the reaction stream by a trap kept at 273 K. Propane conversion was calculated using N_2 as an internal standard. The concentration of products is given as percentage of the dry composition of effluents, including hydrogen, carbon monoxide, carbon dioxide and cracking products (mainly CH_4 and C_2H_4), as well as not reacted propane.

3. Results and discussion

3.1. Catalysts characterization

The results of N_2 adsorption–desorption isotherm measurements are reported in Table 1 and Fig. 1 for both the oxidized (Ox-) and reduced (Red-) catalysts. It is worthy to note that both methods of synthesis lead to a consistent decrease of surface area and porosity of support. This is probably due to the high temperature of calcination adopted for the decomposition of precursors. Moreover, the type of synthesis affects the final morphology and porosity of catalysts. In fact, the catalyst prepared by coprecipitation (C1) shows a higher surface area than the catalyst prepared by Pechini route (C2) and a different pore size distribution (Fig. 1). Fig. 1 points out that the porosity of the C2 catalyst mirrors
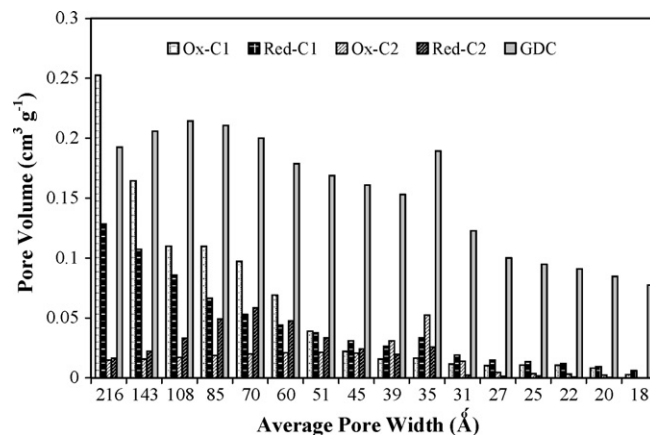

Fig. 1. Correlation between pore volume and average pore size distribution for oxidized and reduced catalysts.

qualitatively the bimodal distribution of the support, with two maxima centred at 35 Å and at 60–70 Å, respectively. On the other hand, quantitatively the fractional values of pore volumes are 10 times lower. In comparison, the C1 sample shows a monotonic distribution with an average pore size of 122 Å. Moreover, the reduction treatment has an opposite effect on the morphology and pore size distributions of the two catalysts: after reduction the C1 sample shows a decrease in surface area of almost 30% along with a reduction of porosity, while for the C2 catalyst a slight increase of surface area and porosity is observed.

The above results suggest that the distribution of the metallic phases obtained with the two methods of deposition is substantially different. It might be possible that via Pechini route, the precursors were mainly adsorbed on the support penetrating into its pores and partially occluding them, with a consequent decrease in surface area of the catalyst. Differently by coprecipitation, rather than a uniform adsorption of the precursors on the support, a good mixing between precursors and carrier occurred forming well mixed, but distinct agglomerates of the three oxides. Thus, the decrease of surface area observed after reduction of the coprecipitated catalyst can be attributed to a slight sintering of the metallic clusters.

Other structural and morphological differences related to the preparation of the catalysts are highlighted by XRD characterization. Fig. 2 compares the diffractograms of the two types of catalysts in oxidized (a, b) and reduced form (c, d). XRD profiles show the peaks of the fluorite phase $Ce_{0.8}Gd_{0.2}O_{1.9}$ (JCPDS-75-0162, not marked) and the Ni phases, NiO (▲, JCPDS-04-0835) and Ni (♦, JPC-01-1258), respectively for the oxidized and for the reduced samples. There is no evidence of rhodium phases, suggesting that they are highly dispersed. The particle size of the support and of the Ni species has been calculated by Scherrer's equation (Table 2). The deposition process affects the size of GDC crystallites; the increase in size is independent on the type of synthesis, and is likely due to the calcination treatment. Conversely, the method of deposition seems to have consequence on the dimension of the NiO and/or Ni crystallites; the Pechini method induces a higher NiO/Ni dispersion with an average crystallite size of 17/18 nm, in comparison to the 26/36 nm size found for the catalyst prepared by coprecipita-
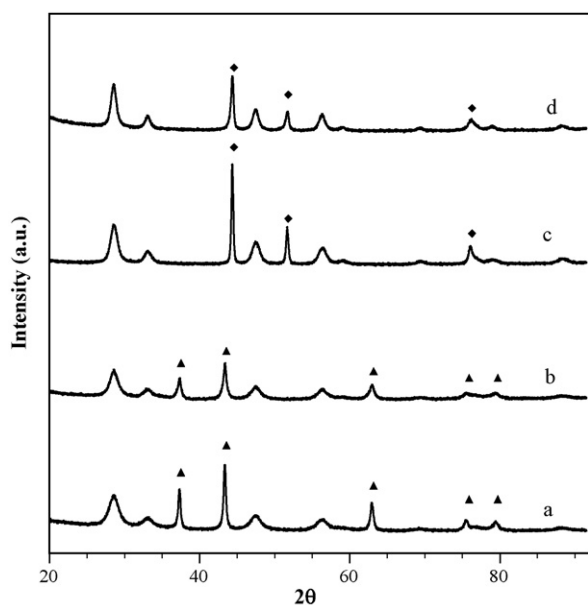
Table 2
XRD results.

Samples	Support particle size[a] (nm)	Metal phase	Metal particle size (nm)
GDC	2.5	–	–
Ox-C1	5.9	NiO	26
Red-C1	7.6	Ni	36
Ox-C2	6.6	NiO	17
Red-C2	9.7	Ni	18

[a] Calculated by Scherrer's equation.

tion. This may be due to a stronger metal–support interaction that would hinder the agglomeration of Ni, since it is well known that, by Pechini synthesis, it is possible to obtain an intermixing of the metal oxide components at molecular level [43–45]. To conclude, it is pointed out that the difference in Ni particle size could be relevant for developing a higher tolerance to carbon, since it has been reported that the size of Ni crystallites is an important factor to control the kinetics of deposition/removal of carbon [46].

High resolution electron microscopy characterization of the samples reduced at 873 K gives confirmation of the structural differences between the catalysts. Moreover, it allows to obtain information regarding the particle size distribution of rhodium and its interaction with the other constituents of the catalyst.
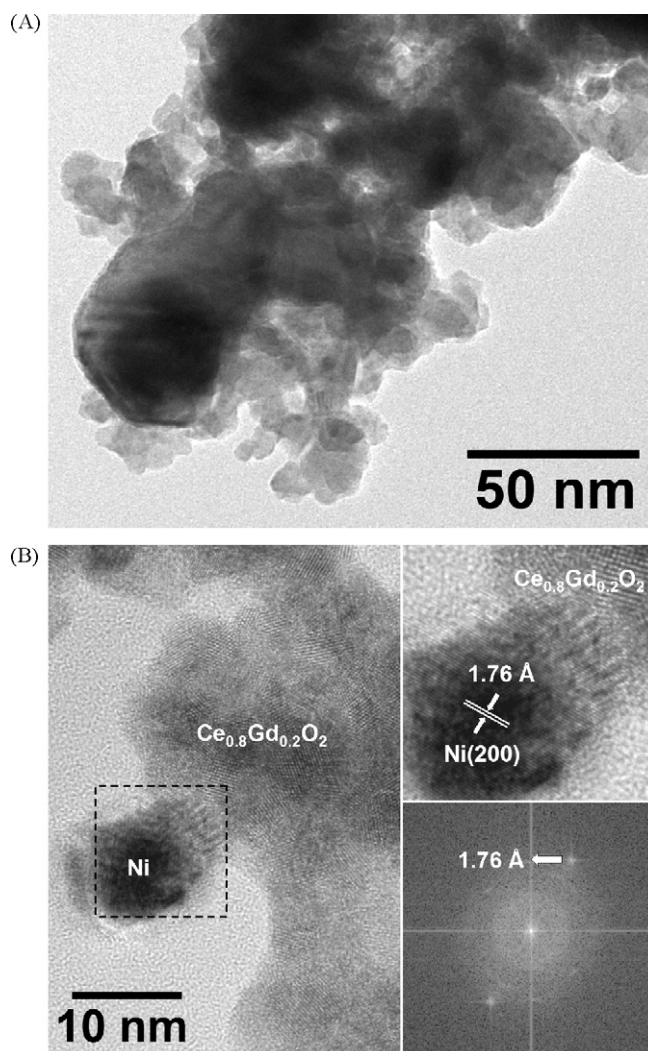

Fig. 3. HRTEM image of sample prepared by coprecipitation: support and Ni identification.

Fig. 2. X-ray diffractograms of (a) Ox-C1, (b) Ox-C2, (c) Red-C1, (d) Red-C2, where "Ox" indicates samples after calcination at 973 K for 5 h, and "Red" samples reduced under 5% H₂ in Ar flow (35 STP cm³ min⁻¹) at 873 K for 1.5 h.

A general view of the sample prepared by coprecipitation is shown in Fig. 3A. The sample is comprised by two types of particles with markedly different sizes; particles of about 6–10 nm correspond to the $Ce_{0.8}Gd_{0.2}O_2$ support, as deduced from ring diffraction patterns, whereas larger particles of about 10–40 nm correspond to metallic nickel particles. An individual Ni crystallite is depicted along $Ce_{0.8}Gd_{0.2}O_2$ particles in Fig. 3B where lattice fringes at 1.76 Å are ascribed to (0 0 2) planes of metallic Ni.

Concerning Rh particles, the sample exhibits an excellent dispersion of Rh crystallites with a mean diameter of 2.4 nm. Fig. 4 corresponds to a detailed, representative HRTEM image. In addition to particles of about 6–10 nm of the $Ce_{0.8}Gd_{0.2}O_2$ support, much smaller particles of ca. 1.5–3.5 nm are very well distributed through the sample. These particles are identified as metallic Rh crystallites. A detailed analysis of one of these particles is included in Fig. 4A. A Fourier transform analysis of the two adjacent areas of the enlarged image corresponding to the support and the small crystallite reveals spots at 3.12 Å corresponding to (1 1 1) planes of $Ce_{0.8}Gd_{0.2}O_2$ support and, for the small crystallite, spots at 2.20 Å corresponding to (1 1 1) crystallographic planes of metallic Rh. An accurate analysis of the FT images indicates that there is no epitaxial growth between Rh and $Ce_{0.8}Gd_{0.2}O_2$. The same applies for
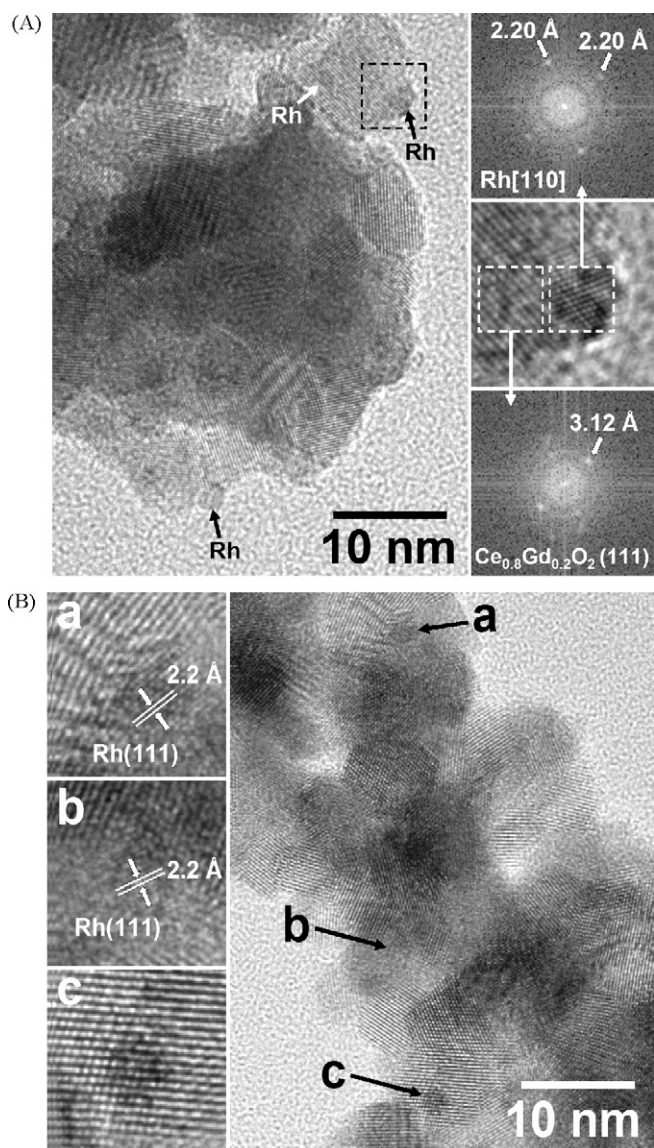

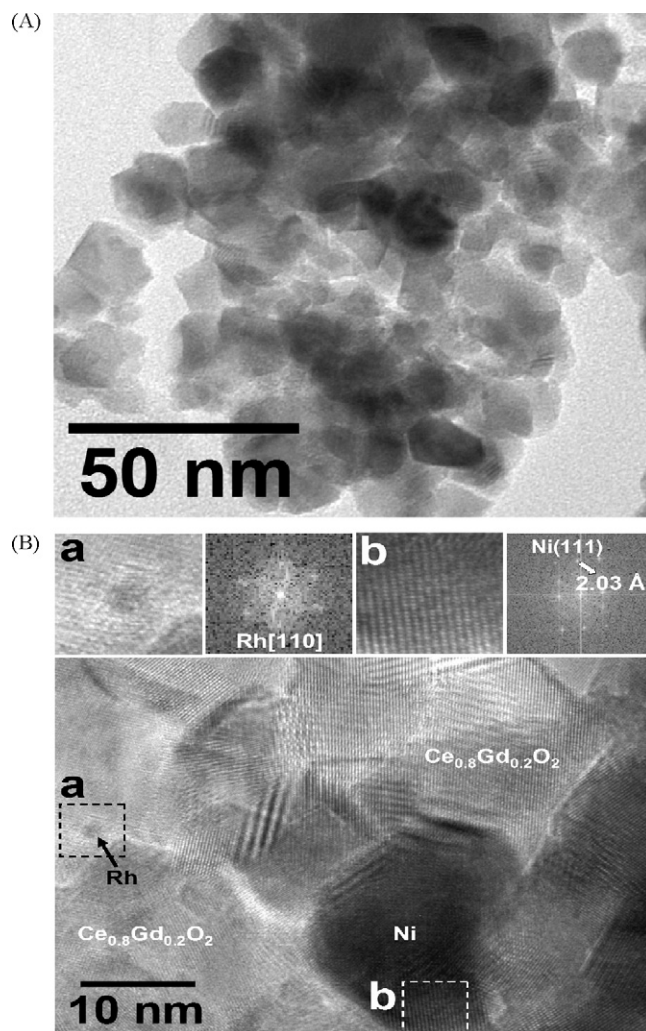**Fig. 4.** HRTEM image of sample prepared by coprecipitation: Rh identification.

Fig. 5. HRTEM image of sample prepared by Pechini method: support and Ni identification.

other Rh crystallites analyzed. Finally, there is no indication for the existence of any Ni–Rh alloy. Given the different particle sizes and electron contrast between $Ce_{0.8}Gd_{0.2}O_2$ and Ni particles it is not possible to discuss about the location of Rh particles, that is, if Rh is mostly supported over $Ce_{0.8}Gd_{0.2}O_2$ or over Ni particles. However, no Rh crystallites have been identified over the smallest Ni particles, suggesting that most Rh is supported over $Ce_{0.8}Gd_{0.2}O_2$ crystallites. Fig. 4B shows another image of this catalyst. Several Rh crystallites are identified on the basis of their lattice fringes at 2.2 Å ascribed to Rh(1 1 1) crystallographic planes.

A general, low-magnification view of the sample prepared by the Pechini method is depicted in Fig. 5A. In this case, $Ce_{0.8}Gd_{0.2}O_2$ support crystallites range from 6 to 15 nm and show very well defined crystallographic facets, which were not observed in the sample synthesized by coprecipitation. Ni particles do not exhibit well defined edges and are much smaller than those present in the sample prepared by coprecipitation. In fact, the size of nickel particles lies in the range 10–25 nm. Rh particles are very well dispersed and, similarly to the sample prepared by coprecipitation, mostly located over the $Ce_{0.8}Gd_{0.2}O_2$ support, not over Ni. The Rh crystallite size distribution is centred at about 2.1 nm, which is relatively lower than that of the coprecipitated sample. However, in this case the size distribution of Rh is slightly broader. Fig. 5B corresponds to a representative HRTEM image of the catalyst, showing the occurrence of a single Rh crystallite oriented along the [1 1 0] crystallographic
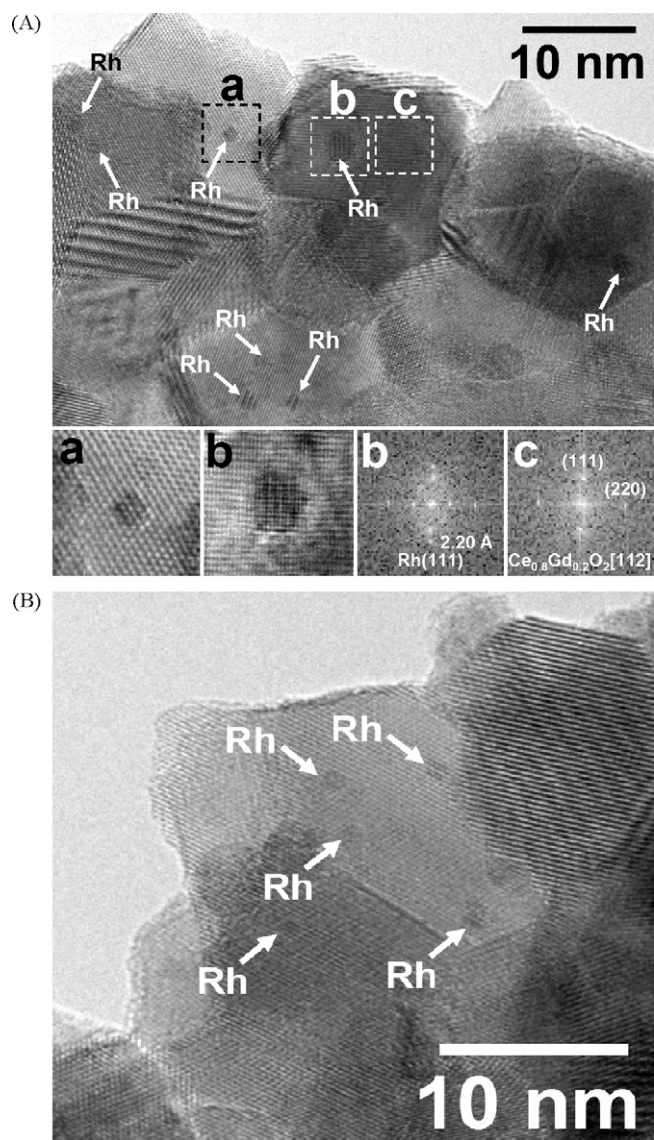
Fig. 6. HRTEM image of sample prepared by Pechini method: Rh identification.
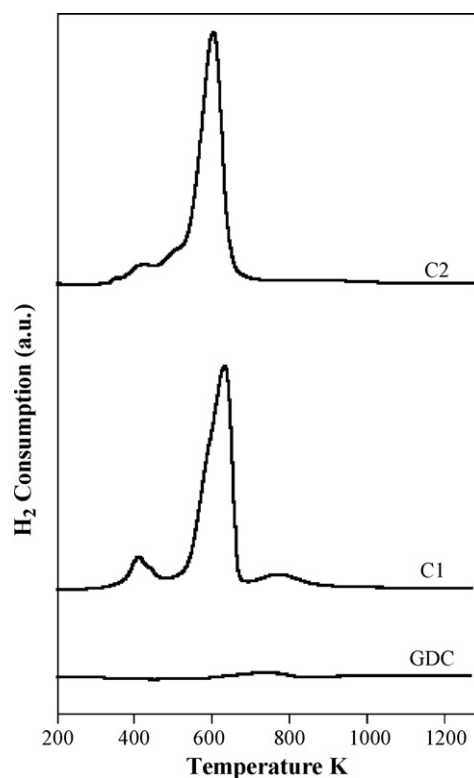

Fig. 7. TPR profiles of fresh Ni–Rh/CGD catalysts. C1, catalyst prepared by coprecipitation; C2, catalyst prepared by Pechini method; GDC, support calcined at 773 K.

direction (inset labeled "a" and the corresponding FT image) and a Ni particle (inset "b" and the corresponding FT image) embedded with the $Ce_{0.8}Gd_{0.2}O_2$ support. Another representative HRTEM image showing the excellent dispersion of numerous Rh crystallites is shown in Fig. 6A. Enlargements of Rh crystallites labeled "a" and "b" are enclosed, showing the occurrence of an epitaxial relationship with the $Ce_{0.8}Gd_{0.2}O_2$ crystallites of the support. The FT image of area "b" shows spots at 2.20, 3.12, and 1.91 Å in addition to Moiré signals. Spots at 3.12 and 1.91 Å correspond to (1 1 1)

and (2 2 0) crystallographic planes of the $Ce_{0.8}Gd_{0.2}O_2$ support, as demonstrated by the analysis of area labeled "c" corresponding to the support alone. Spots at 2.20 Å correspond to (1 1 1) crystallographic planes of Rh. These spots are aligned with those ascribed to (1 1 1) planes of the $Ce_{0.8}Gd_{0.2}O_2$ support crystallite, whereas those of (2 2 0) are aligned with the Moiré spots arising from the interference between the $Ce_{0.8}Gd_{0.2}O_2$ and Rh crystallites. In most cases where lattice fringes corresponding to Rh and the underlying $Ce_{0.8}Gd_{0.2}O_2$ support have been recorded there is evidence for epitaxial relationship. Fig. 6B shows another representative HRTEM image of the sample exhibiting an excellent dispersion of Rh crystallites. Even in this micrograph, it is possible to observe Moiré fringes originating from epitaxial growth.

Differences into the interaction between metal and support and into the rhodium dispersion can be also deducted from a careful examination of the results of temperature programmed measurements. Fig. 7 shows the TPR profiles for the coprecipitation (C1) and Pechini (C2) samples, together with that of the support (GDC). Both reduction patterns have a main peak in the range of 523–723 K attributable to the reduction of bulk-like NiO [47]. According to literature [36], the peaks observed in the 323–523 K range are

Table 3
TPR quantitative analysis.

Reducible species	Percentage reduction[a] (%)					H_2 consumption[b] (mol g^{-1})
	C1	C2	R-C1	R-C2	GDC	
Total oxides	75.6	68	74.9	72.5	32.5	9.54E−03
$NiO + Rh_2O_3$	79.7	77.0	nd	nd	–	8.39E−03
NiO	76.7	73.0	nd	nd	–	7.67E−03
Rh_2O_3	110	116	nd	nd	–	7.29E−04
$Ce_{0.8}Gd_{0.2}O_2$	45	6	nd	nd	–	1.15E−03

nd: not determined.

[a] Calculated as ratio between the measured and the calculated consumption of H_2.

[b] Calculated taking into account the weight percent metal loading: 45% Ni, 5% Rh, 50% GDC.
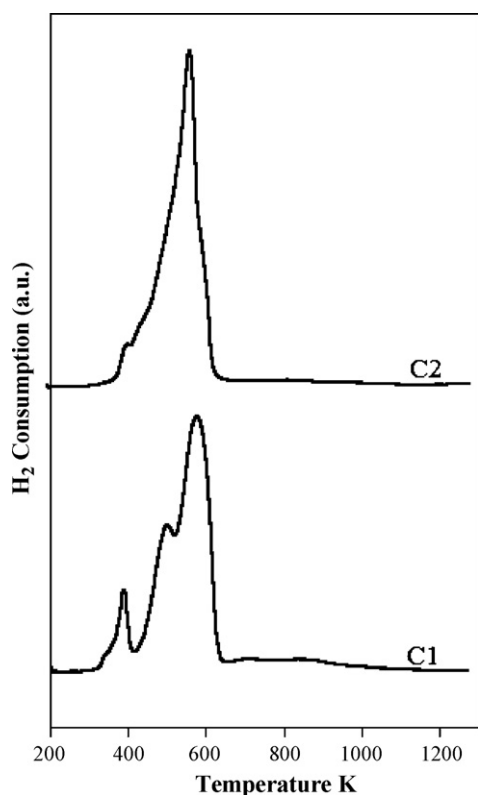
Table 4
H$_2$ chemisorption results.

Samples	Temperature of reduction (K)	Cumulative volume adsorbed (mL g^{-1})	Metal dispersion (%)	Metallic surface area (m^2 g^{-1} cat)	Metallic surface area (m^2 g^{-1} metal)	Active particle size (nm)
C1	453	3.41	62.6	13.8	275.6	1.7
C2	503	3.23	59.3	13.0	260.9	1.8
C2	453[a]	1.82	66.6	7.4	293.3	1.6
C2	503	1.40[b]	51.6[c]	5.6	nd	2.1

nd: not determined.

[a] Calculated taking into account 50% reduction of total Rh oxide.

[b] Calculated as difference of the cumulative volume adsorbed after reduction at 503 and 453 K.

[c] Calculated taking into account 50% reduction of total Rh oxides.

related to the reduction of rhodium oxides, while the band in the 673–873 K range is attributed to GDC reduction. The TPR profiles of the two samples are quite similar; however there is a difference in their shape especially in the range of 323–523 K. For the coprecipitated catalyst, the low temperature peak is well distinct from the NiO reduction peak, while for the Pechini catalyst the corresponding peak shows a broader shoulder at higher temperature that slightly overlaps with that of NiO. Since the rhodium oxides reduction occurs in the range of 323–523 K, different TPR patterns in this region could be due to a different distribution and interaction between rhodium, nickel and GDC.

Table 3 (first two columns) shows the quantitative analysis of the TPR measurements, calculated by deconvolution and integration of the TPR profiles in three or four components according to the peak attributions discussed above. The percentages refer to the theoretical amount reported on the last column. It is interesting to note that the total degree of reduction is lower for the sample prepared via Pechini route (C2) and this difference is mainly due to a minor reduction of the support. On the other hand, the percentage of total metal reduction is almost the same for both catalysts. The integrated area of the low temperature peaks corresponds to a

H$_2$ consumption higher than the amount needed for the complete reduction of Rh$_2$O$_3$ to Rh, suggesting that rhodium may promote the reduction of the other catalyst components through hydrogen spillover. Conversely, under TPR conditions, it is not possible to obtain a full reduction of the NiO. The lower degree of reduction of the support for the catalyst prepared by Pechini method could be correlated to the diverse morphological and structural characteristics with respect to the catalyst prepared by coprecipitation. As shown by HRTEM images, this catalyst has larger and well faced Gd$_{0.8}$Ce$_{0.2}$O$_2$ crystallites, which are probably less reducible. There is also the possibility that in the case of Pechini catalyst the phenomenon of spillover promotes the reduction of Ge$_{0.80}$Ce$_{0.2}$O$_2$ at lower temperature. In that case the quantitative evaluation of the degree of reduction of the single components must be taken with some reserve due to the impossibility to separate each other the corresponding peaks.

Fig. 8. TPR profiles of catalysts after redox treatment: reduction at 873 K for 2 h and successive oxidation at 773 K for 1 h.
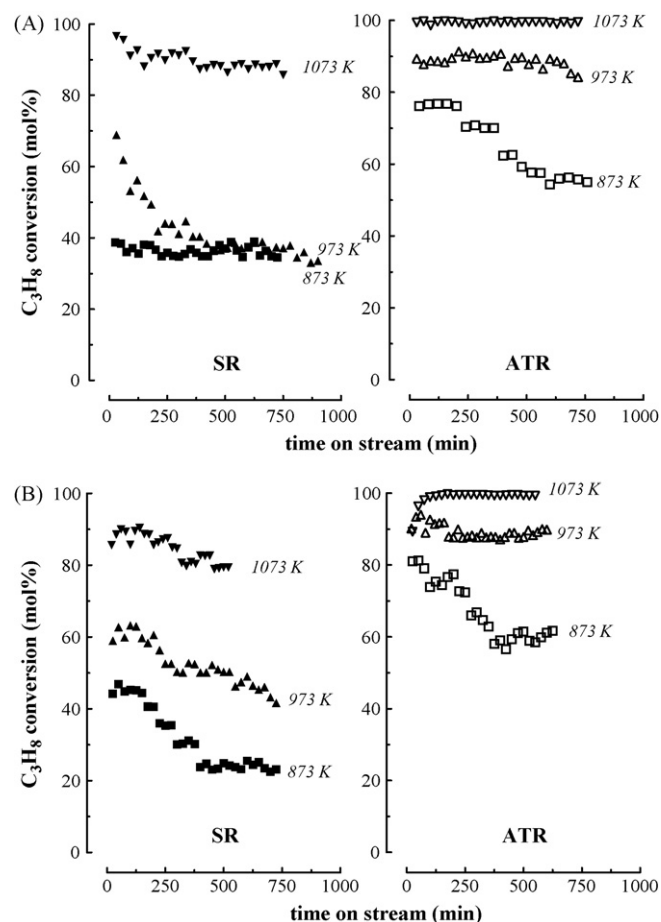
Fig. 9. Propane conversion at different temperatures as a function of time on stream in SR and ATR conditions: (A) catalyst: C1; (B) catalyst: C2.

Since the reduction of rhodium oxide occurs consistently at a lower temperature than that of NiO, the average dispersion of rhodium was evaluated by selective H_2 chemisorption measurements after reduction and degassing steps at 453 K and at 503 K for the coprecipitation and the Pechini samples, respectively. The corresponding results are reported in Table 4. Both syntheses lead to a very fine dispersion of rhodium, which is in close agreement with the HRTEM findings. At low temperature the TPR profile of catalyst prepared by Pechini shows two components that can be correlated to a bimodal particle size distribution of rhodium. The H_2 chemisorption measurements, carried out after successive reduction at 453 and 503 K, allow estimating the average size of the two contributions, one constituted by particles smaller than 2 nm at low temperature and another one, at higher temperature, with particles larger than 2 nm. However, on the basis of HRTEM results, the two components of the Rh peak could be differently explained and rather correlated with a different dimensional configuration of the rhodium species. In particular, for the Pechini catalyst it is possible to distinguish two types of rhodium particles, the first one only loosely bounded with NiO/GDC, and the other well interfaced with GDC by an epitaxial interaction (see Fig. 6). Recently Ferrandon and Krause [36] reported analogous results for their systems. The appearance, after ageing, of an additional peak, beside the one observed on the Rh/GDC fresh catalyst, was explained by a change of morphology and of metal/support interaction for the rhodium particles. In this case the low temperature peak was attributed to sintered particles with a three dimensional morphology, while the peak at higher temperature was related to bi-dimensional flat particles, strongly interacting with the support.

On the other hand, the differences into the profile of reduction at low temperature can suggest also a stronger interaction between the noble metal and nickel oxide in the case of the catalyst prepared by Pechini method. That would affect the reciprocal reduction of the metals [48]. This interpretation is supported by the fact that NiO reduction is shifted at a lower temperature than that of the coprecipitated catalyst. In fact, a tight interconnection between the noble metal and Ni would promote the Ni reduction at lower temperature due to spillover [49].

Since SR and ATR reactions imply the use of a redox atmosphere, we investigated the stability of the catalysts versus a redox treatment by a TPR experiment performed after exposure to H_2/Ar (2 h at 873 K) and air (1 h at 773 K). Fig. 8 shows the TPR profiles of the reduced–oxidized samples; it is interesting to note that, although the total degree varies only of few points percent (see Table 3, R-C# samples), the TPR profiles change in shape in comparison to the fresh catalysts. For both catalysts, the NiO reduction peak rises at lower temperature and there is a consistent merging of the components, more pronounced for the Pechini catalyst. This suggests that, independently on the method of synthesis, redox treatments induce some change in the interaction between Ni and Rh. These findings would require further investigations because of possible implications in the long term catalytic activity and stability ver-
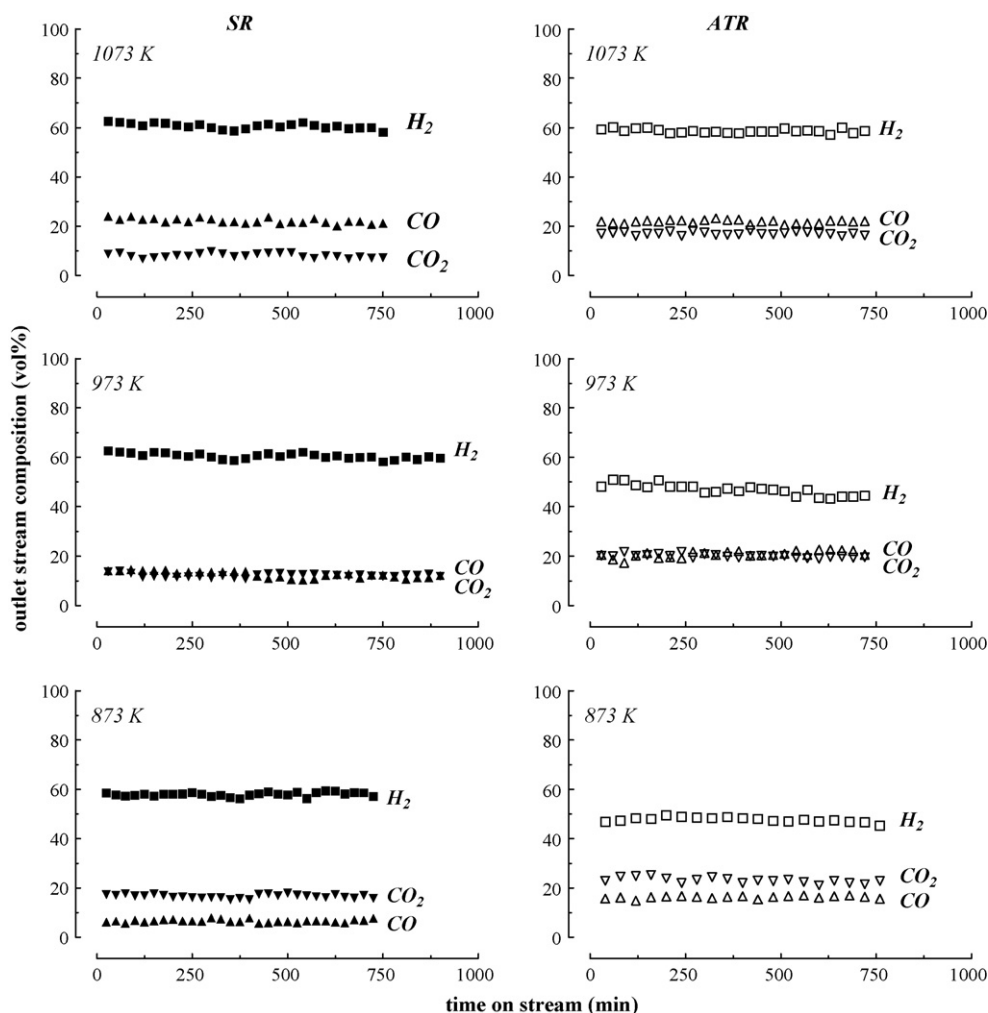

Fig. 10. Product distribution at different temperatures as a function of reaction on stream in SR and ATR conditions: catalyst C1.
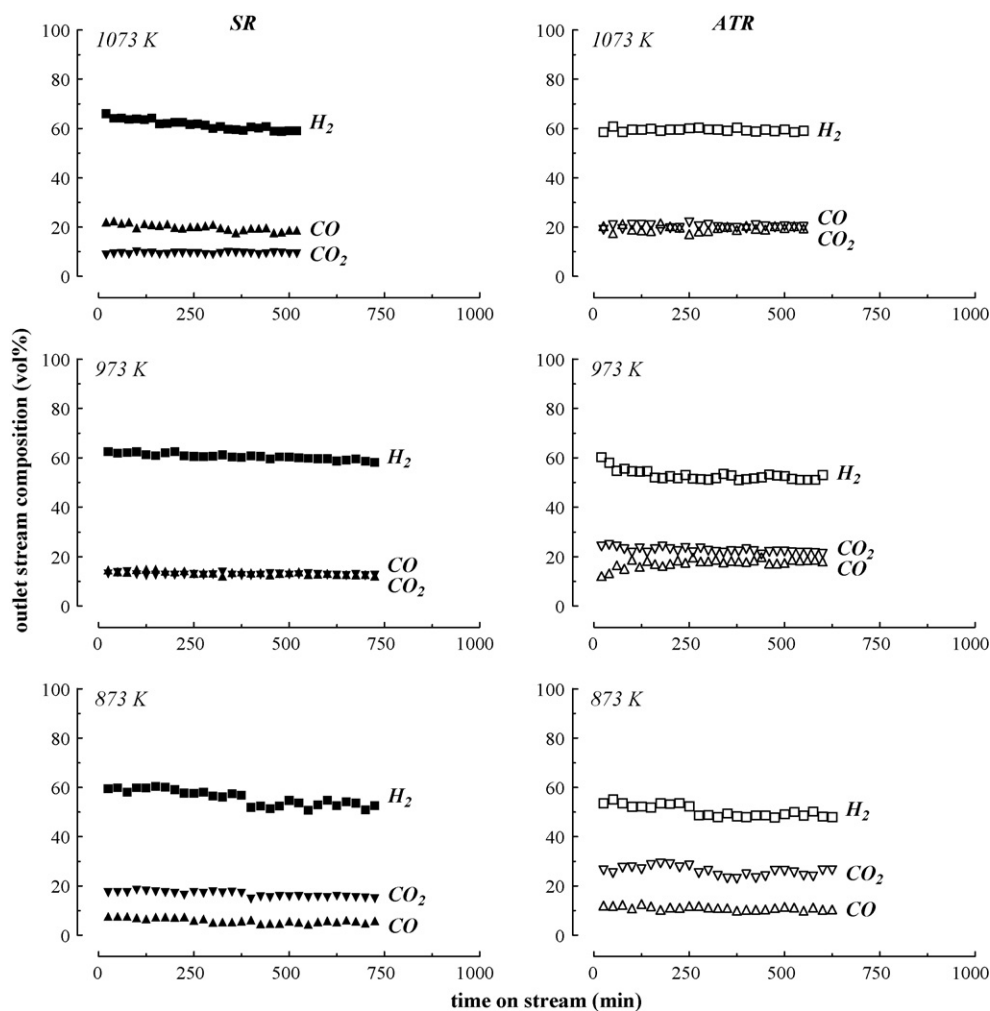
Fig. 11. Product distribution at different temperatures as a function of reaction on stream in SR and ATR conditions: catalyst C2.

sus coke formation, as well as in the regeneration processes of the catalysts.

3.2. Catalytic activity

The catalytic behaviour of Ni–Rh/GDC catalysts, in terms of propane conversion versus reaction time at different reaction temperatures, under both SR and ATR conditions, is shown in Fig. 9. The initial propane conversion increases with reaction temperature for both SR and ATR (from 40–45% to 85–95% in SR and from 80% to 100% in ATR). Under ATR conditions the propane conversion is very high and the two catalysts show the same behaviour: both catalysts exhibit a good stability at 973 and 1073 K, while at 873 K they show a deactivation of 20–28% in the first 6 h of reaction, then they stabilize to a conversion value of 58–60%. In SR, the two catalysts show similar conversion at the same temperature and lower than in ATR, suggesting that oxygen plays a decisive role in promoting catalyst activity. Although the initial conversion of the two catalysts is similar for a given temperature, they are different in term of deactivation trend. At 873 K the catalyst prepared by coprecipitation (C1) is stable (Fig. 9A), with an average conversion of 36%, while for the catalyst prepared by Pechini method (C2) (Fig. 9B) the initial conversion is slightly higher (45%), but it decreases with time especially after the first 3 h of reaction, reaching a stable value of 23% after 6 h. At 973 K, both the catalysts deactivate. The conversion of the Pechini catalyst decreases gradually from 61% (average value measured in the first 3 h) to 50% after 8 h of reaction, stabiliz-

ing only at the end. Conversely, the activity of the sample prepared by coprecipitation shows an exponential decrease in the first 3 h, but it stabilizes more rapidly to a value of 37% after 6 h. At 1073 K in SR, the two catalysts are very similar in terms of conversion and deactivation trends; at the start of the experiment, conversion is almost complete (>85%) and decreases only 10% in 8 h.

Product distribution for both catalysts depends on operating conditions (see Figs. 10 and 11). In fact, a comparison of selectivity data in SR and ATR at the same reaction temperature shows that the presence of oxygen in the reaction stream contributes to a slight decrease in hydrogen selectivity, mainly at 973 and 873 K (from 60 to 50% and from 58% to 48%, respectively). At 1073 K, H_2 selectivity does not change significantly; under both SR and ATR conditions, it is close to 60%. It should be noted that, even when catalysts deactivate (mainly at 873 K), product selectivity does not change over time.

In terms of H_2 productivity (Fig. 12), further to observe that the hydrogen yield drastically increases with reaction temperature, ATR condition seems to be more adequate to obtain more hydrogen. However, considering that in reforming processes devoted to SOFC purposes, an important issue is also the attainment of high syngas ($CO + H_2$) yields, the data has been rearranged in terms of syngas production as a function of reaction temperature (Fig. 13). Syngas production linearly increases with reaction temperature under both SR and ATR conditions but, contrarily to what observed in terms of H_2 yield, the difference between catalysts is negligible.
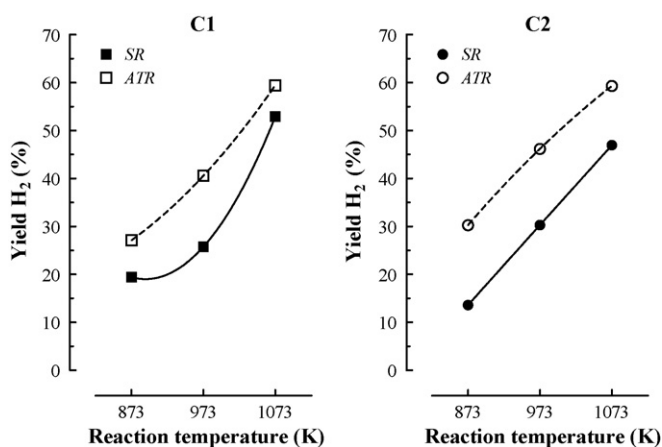
Fig. 12. Hydrogen yield vs. reaction temperature in SR and ATR conditions.

Fig. 13. Selectivity to syngas as a function of reaction temperatures in SR and ATR conditions: SR (▲, C1; ●, C2); ATR (△, C1; ○, C2).

In order to understand the causes of deactivation, the used samples were investigated by transmission electron microscopy. TEM images of catalyst C1 shown in Figs. 14 and 15 denote the existence of marked differences in terms of extent and morphology of the carbon deposited. In particular, in ATR coke formation decreases as a result of oxygen presence in the feed, while in SR the formation of huge amounts of multi-walled carbon nanotubes occurred. At 1073 K, there was no coke formation under both SR and ATR conditions, even though the structure of the catalyst changed significantly; particularly, the support tends to aggregate, losing its porous structure and becoming more compact. In addition, sintering of metal particles, from 10 to 30 nm, occurs. TEM images of the C2 catalyst
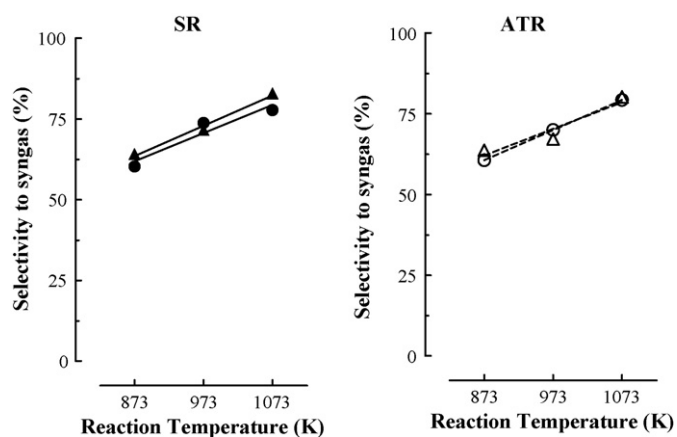
shown in Figs. 16 and 17 confirm in general what has been observed for the C1 sample; especially after SR reaction, the amount of coke formed is much higher, in particular at 873 and 973 K.

To gain information on whether or not the nature of catalysts affects the formation and removal of carbon, thermo-gravimetric measurements in air flow were performed on samples treated under dry 8.6% C_3H_8/N_2 flow (150 STP cm^3 min^{-1}) for 1 h at 873 and 973 K. Conditions in this experiment were different from those used in the catalytic tests, which were chosen on the basis of thermodynamic considerations in an effort to avoid carbon formation; however, the results obtained can provide useful information on the intrinsic stability of the two catalysts versus the formation of
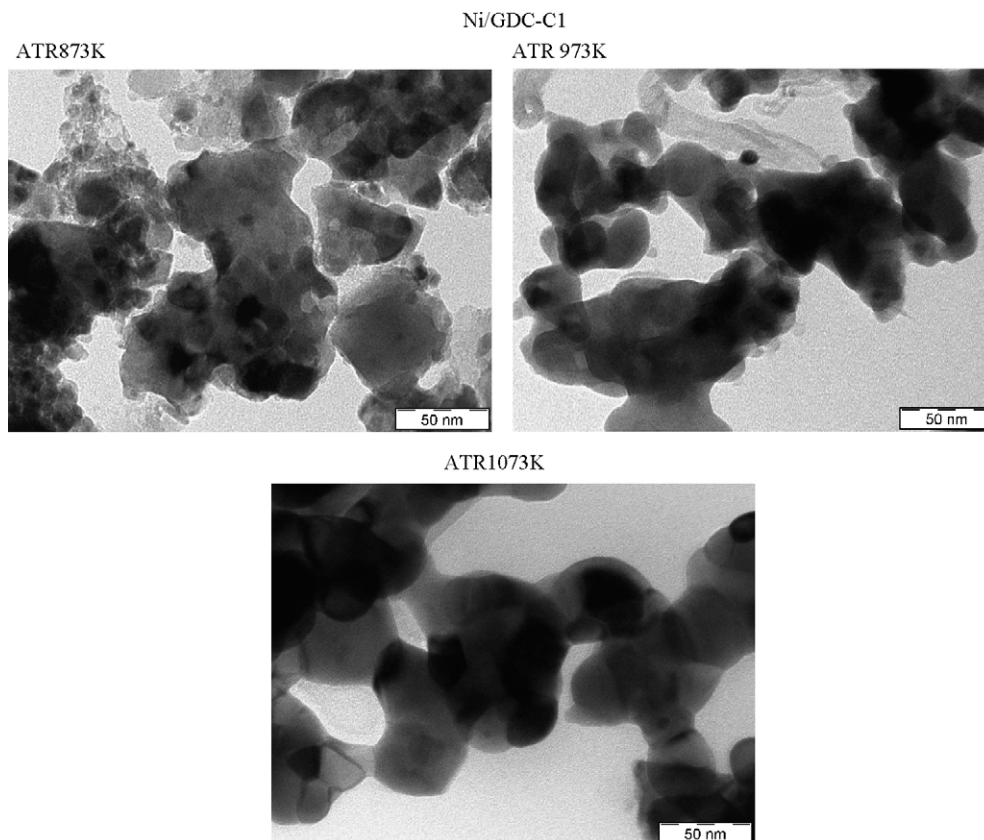

Fig. 14. TEM images of C1 catalyst used in ATR conditions at different reaction temperatures.
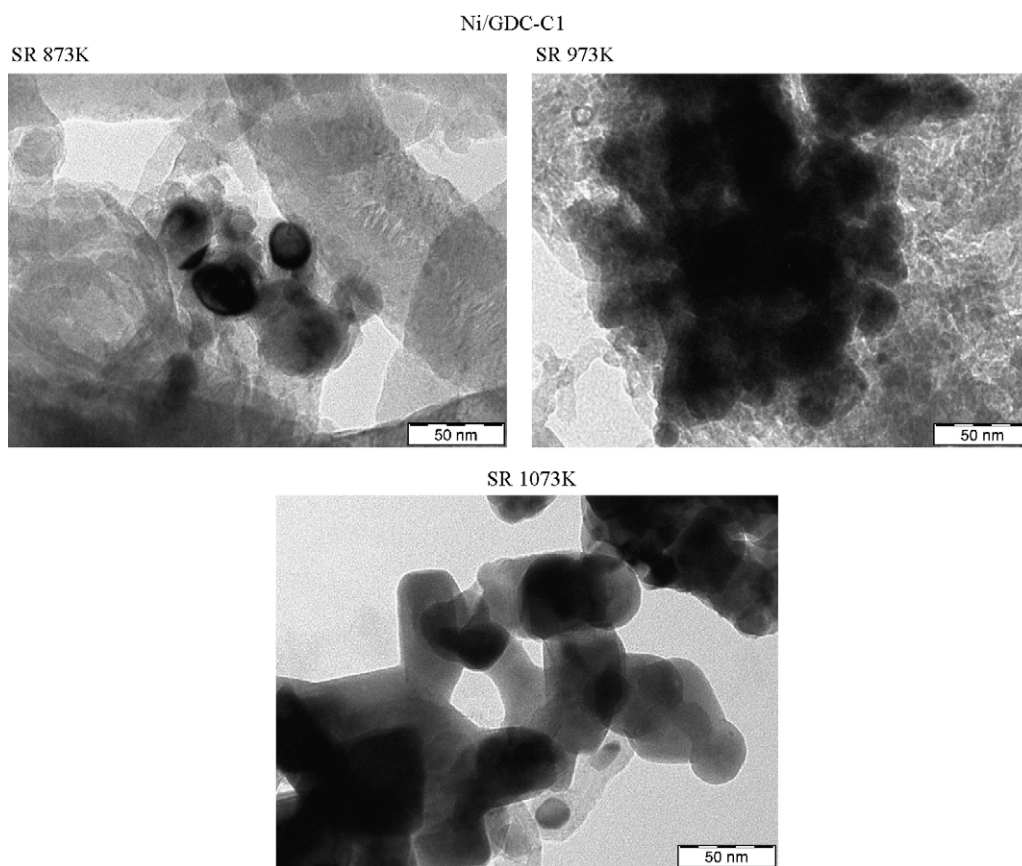
Ni/GDC-C1

SR 873K

SR 973K

SR 1073K

Fig. 15. TEM images of C1 catalyst used in SR conditions at different reaction temperatures.

Ni/GDC-C2

ATR 873K

ATR 973K

ATR 1073K
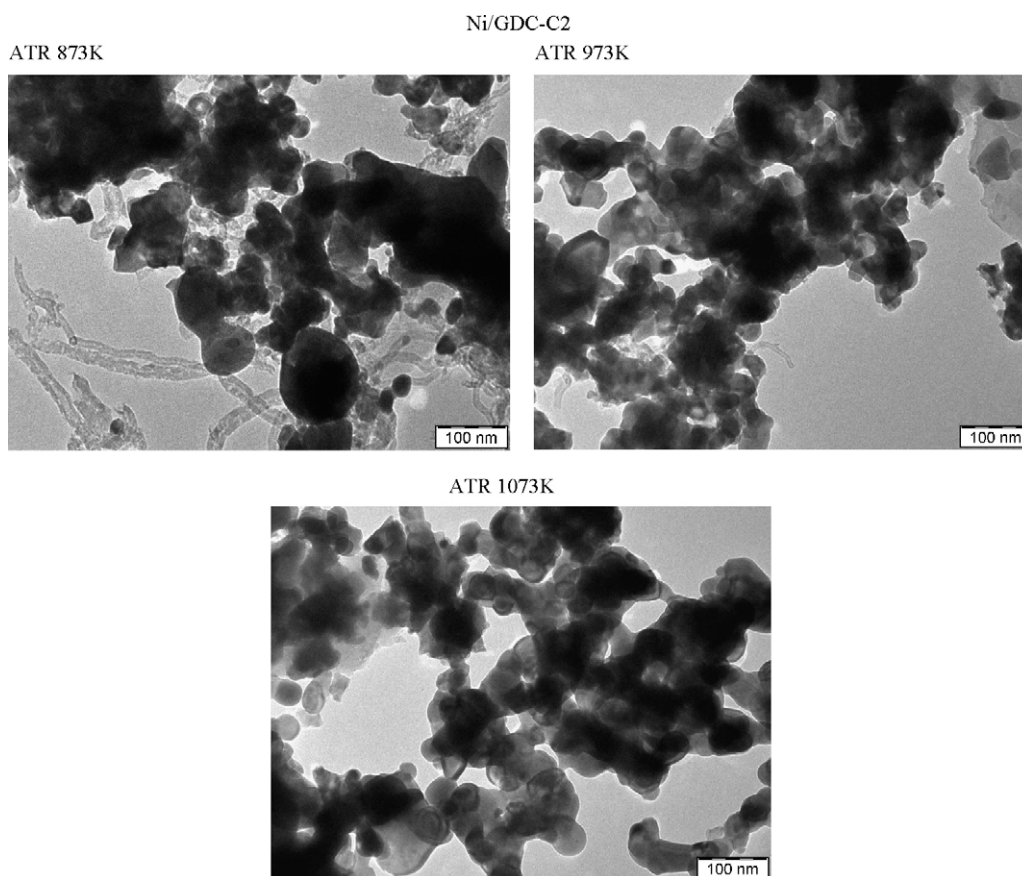
Fig. 16. TEM images of C2 catalyst used in ATR conditions at different reaction temperatures.
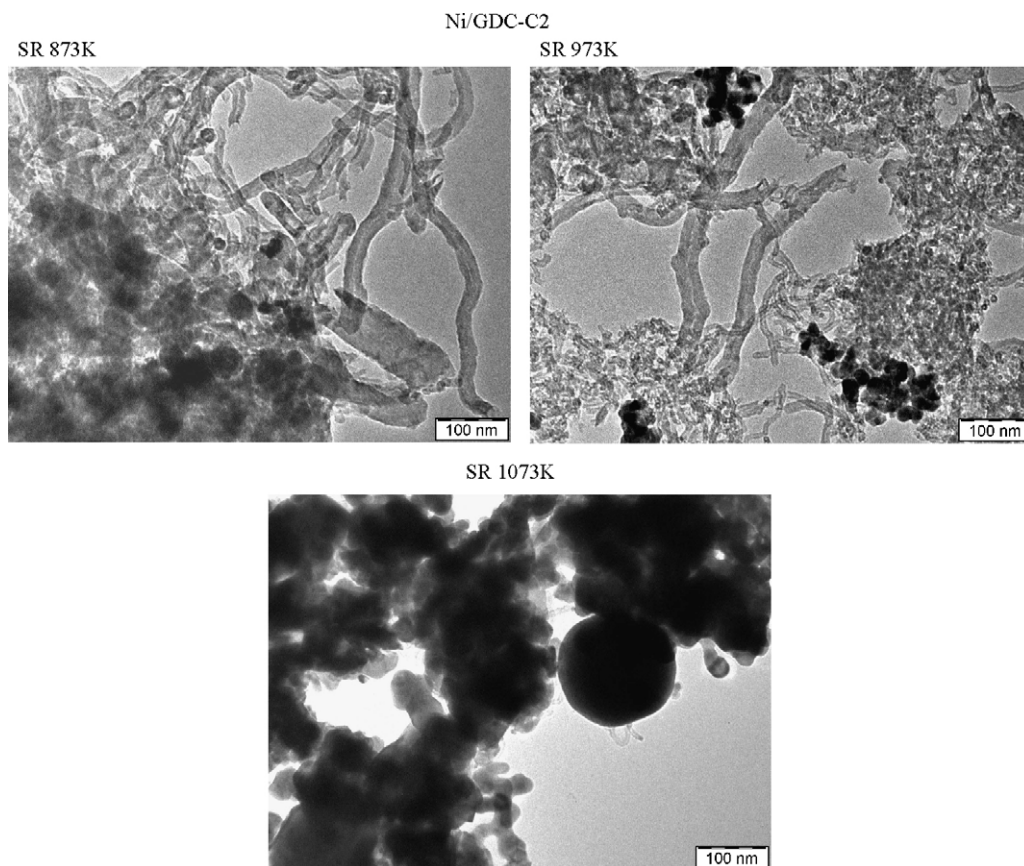
Ni/GDC-C2

SR 873K

SR 973K

SR 1073K

Fig. 17. TEM images of C2 catalyst used in SR conditions at different reaction temperatures.

carbon. Fig. 18 shows the TG patterns of the samples prepared by coprecipitation (C1, solid lines) and Pechini route (C2, dotted lines), treated at 873 K (grey lines) and at 973 K (black lines). The catalyst C2 accumulates more carbon than the sample C1; however, combustion occurs at lower temperature. Moreover, the C1 catalyst had a more complex profile with two steps of decomposition. The CHNS elemental analysis over the deactivated samples reported in Fig. 15 also confirms that coke forms on the Pechini catalyst at a much
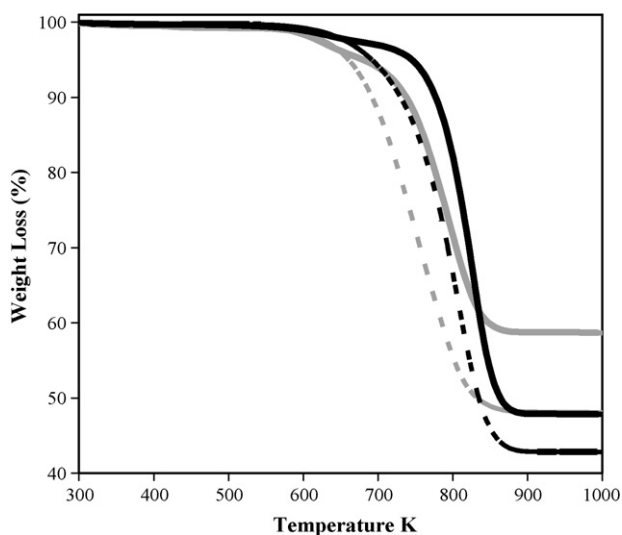
higher rate. Furthermore, under ATR conditions coke formation on both catalysts is significantly lower than in SR; for the Pechini catalyst, it takes place at a rate approximately 3 times higher than that of the catalyst prepared by coprecipitation.

In a recent paper we have already inferred that the change in coke formation mechanism is depending upon several factors, like metal particle diffusion flux area, particle thickness and driving force for carbon diffusion [50]. The low thermal stability of propane at temperatures higher than 773 K should also be taken into consideration for coke formation since by propane cracking the formation of elementary carbon and olefins is favoured.

From the physico-chemical characterization of catalysts reported in the previous paragraph, it emerges that with Pechini method, even if the total surface area of GDC is lower than that of coprecipitated catalyst, Rh and Ni are better dispersed on carrier surface. Furthermore, this catalyst is better reducible since the interaction Rh–Ni is favoured by a more intimate contact.

Unfortunately, such peculiarities seem to negatively reflect on coke formation rate (see Fig. 19). A recent paper [51] reported that a pre-eminent role in the coke formation mechanism is played by metal particle size. It has been found that Ni catalysts characterized by large metal particles feature the longest catalytic life for methane decomposition on Ni/SiO$_2$, since these particles allow to work with high carbon diffusion rate promoting the formation of filamentous carbon. In fact, the carbon formation is straight depending upon the driving force controlling the carbon diffusion process. At steady state, it can be assumed that the coking rate equals the rate of carbon diffusion through the metal particle. With propane as reactant, we found that coke formation occurs with higher rate on smaller Ni particles and this result should indicate that, in the present case, the propane cracking reaction should be considered as the pre-eminent
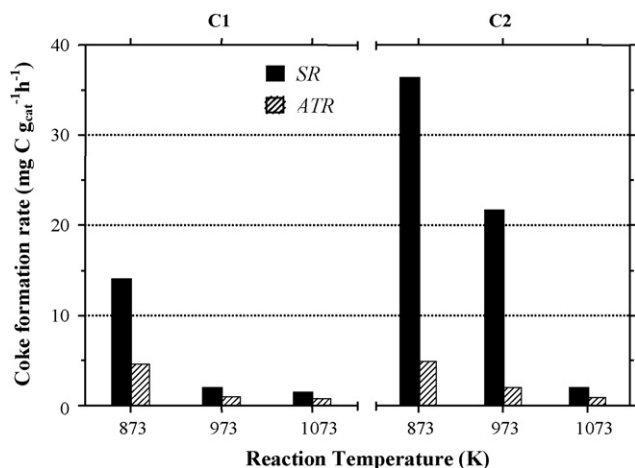

Fig. 18. Thermo-gravimetric profiles of C1 (—) and C2 (- - -) at 873 K (grey lines) and 973 K (black lines).

Fig. 19. Coke formation rate on C1 and C2 catalysts in SR and ATR conditions at different reaction temperatures.

phenomenon in promoting coke formation. The same behaviour has been already observed for other type of catalysts [52,53].

4. Conclusions

Ni–Rh/GDC prepared by coprecipitation and Pechini methods are active catalysts for hydrogen production by SR and ATR of propane. Both catalysts deactivated under SR conditions, their deactivation trends depending on reaction temperature (the higher the reaction temperature, the lower the deactivation). Under ATR condition, both catalysts were stable at 973 and 1073 K, and coke formation was drastically reduced due to the presence of oxygen, which favours the carbon residue gasification. The catalyst prepared by coprecipitation was less affected by coke formation. Such a result is justified considering that coke formation rate is strictly depending upon Ni dispersion; the higher is the Ni dispersion, the higher is the coke formation rate. Propane cracking reaction was considered the pre-eminent phenomenon responsible for coke formation.

Acknowledgements

References

[1] A.F. Ghenciu, Curr. Opin. Solid State Mater. Sci. 6 (2002) 389–399.
[2] R. Farrauto, S. Hwang, L. Shore, W. Ruettinger, J. Lampert, T. Giroux, Y. Liu, O. Ilinich, Annu. Rev. Mater. Res. 33 (2003) 1–27.
[3] K. Eguchi, H. Kojo, T. Takeguchi, R. Kikuchi, K. Sasaki, Solid State Ionics 152/153 (2002) 411–416.
[4] S.H. Clarke, A.L. Dicks, K. Pointon, T.A. Smith, A. Swann, Catal. Today 38 (1997) 411–423.
[5] L.J. Gauckler, D. Beckel, B.E. Buergler, E. Jud, U.P. Muecke, M. Prestat, J.L.M. Rupp, J. Richter, CHIMIA 58 (2004) 1–11.
[6] N.Q. Minh, Solid State Ionics 174 (2004) 271–277.
[7] M. Mogensen, K. Krammer, Annu. Rev. Mater. Res. 33 (2003) 321–333.
[8] R.J. Gorte, AIChE J. 51 (2005) 2377–2381.
[9] S. McIntosh, R.J. Gorte, Chem. Rev. 104 (2004) 4845–4865.
[10] J.R. Rostrup-Nielsen, J. Sehested, J.K. Nørskov, Adv. Catal. 47 (2002) 65–139.
[11] J. Maček, B. Novosel, M. Marišenk, J. Eur. Ceram. Soc. 27 (2007) 487–491.
[12] C.M. Finnerty, N.J. Coe, R.H. Cunningham, R.M. Ormerod, Catal. Today 46 (1998) 137–145.
[13] H. Sumi, K. Ukai, Y. Mizutani, H. Mori, C. Wen, H. Takahashi, O. Yomamoto, Solid State Ionics 174 (2004) 151–156.
[14] K. Ke, A. Gunji, H. Mori, S. Tsuchida, H. Takahashi, K. Ukai, Y. Mizutani, H. Sumi, M. Yokoyama, K. Waki, Solid State Ionics 177 (2006) 541–547.
[15] S. Zha, A. Moore, H. Abernathy, M. Liu, J. Electrochem. Soc. 151 (2004) A1128–A1133.
[16] T. Takeguchi, R. Kikuchi, T. Yano, K. Eguchi, K. Murata, Catal. Today 84 (2003) 217–222.
[17] T. Iida, M. Kawano, T. Matsui, R. Kikuchi, K. Eguchi, J. Electrochem. Soc. 154 (2007) B234–B241.
[18] A.L. Dicks, J. Power Sources 71 (1998) 111–122.
[19] M. Krumpelt, T.R. Krause, J.D. Carter, J.P. Kopasz, S. Ahmed, Catal. Today 77 (2002) 3–16.
[20] F. Chen, S. Zha, J. Dong, M. Liu, Solid State Ionics 166 (2004) 269–273.
[21] K. Foger, K. Ahmed, J. Phys. Chem. B 109 (2005) 2149–2154.
[22] Z. Zhan, S.A. Barnett, Solid State Ionics 176 (2005) 871–879.
[23] T. Hibino, A. Hashimoto, M. Yano, M. Suzuki, M. Sano, Electrochim. Acta 48 (2003) 2531–2537.
[24] M. Lo Faro, D. La Rosa, G. Monforte, V. Antonucci, A.S. Aricò, P. Antonucci, J. Appl. Electrochem. 37 (2007) 203–208.
[25] N. Laosiripojana, W. Sangtongkitcharoen, S. Assabumrungrat, Fuel 85 (2006) 323–332.
[26] N. Laosiripojana, S. Assabumrungrat, J. Power Sources 158 (2006) 1348–1357.
[27] S. Ayabe, H. Omoto, T. Utaka, R. Kikuchi, K. Sasaki, Y. Teraoka, K. Eguchi, Appl. Catal. A: Gen. 241 (2003) 261–269.
[28] A. Beretta, P. Forzatti, Chem. Eng. J. 99 (2004) 219–226.
[29] B. Silberova, H.J. Venvik, A. Holmen, Catal. Today 99 (2005) 69–76.
[30] R.P. O'Connor, E.J. Klein, L.D. Schmidt, Catal. Lett. 70 (2000) 99–107.
[31] D. Shekhawat, T.H. Gardner, D.A. Berry, M. Salazar, D.J. Haynes, J.J. Spivey, Appl. Catal. A: Gen. 311 (2006) 8–16.
[32] P.M. Torniainen, X. Chu, L.D. Schmidt, J. Catal. 146 (1994) 1–10.
[33] J. Thormann, P. Pfeifer, U. Kunz, K. Shulbert, Int. J. Chem. React. Eng. 6 (2008) P1.
[34] N. Hotz, M.J. Stutz, S. Loher, W.J. Stark, D. Poulikakos, Appl. Catal. B: Environ. 73 (2007) 336–344.
[35] S. Bernal, J.J. Calvino, J.M. Gatica, C.L. Cartes, J.M. Pintado, in: A. Trovarelli (Ed.), Catalysis by Ceria and Related Materials, Imperial College Press, London, 2002, pp. 85–168.
[36] M. Ferrandon, T. Krause, Appl. Catal. A: Gen. 311 (2006) 135–145.
[37] U. Hennings, R. Reimert, Appl. Catal. A: Gen. 337 (2008) 1–9.
[38] T. Inui, Stud. Surf. Sci. Catal. 77 (1993) 17–26.
[39] T. Inui, K. Saigo, Y. Fujii, K. Fujioka, Catal. Today 26 (1995) 295–302.
[40] S. Irusta, L.M. Cornaglia, E.A. Lombardo, J. Catal. 210 (2002) 263–272.
[41] C. Crisafulli, S. Scirè, S. Minicò, L. Solarino, Appl. Catal. A: Gen. 225 (2002) 1–9.
[42] F. Basile, G. Fornasari, F. Trifirò, A. Vaccari, Catal. Today 77 (2002) 215–223.
[43] M.P. Pechini, US Patent 3,330,697 (1967).
[44] T. Razpotnik, J. Maček, J. Eur. Ceram. Soc. 27 (2007) 1405–1410.
[45] S. Bariso, M. Battagliarin, S. Daolio, M. Fabrizio, E. Miorin, P.L. Antonucci, S. Candamano, V. Modafferi, E.M. Bauer, C. Bellito, G. Righini, Solid State Ionics 177 (2007) 3473–3484.
[46] H.S. Bengaard, J.K. Norskov, J. Sehested, B.S. Clausen, L.P. Nielsen, A.M. Molenbroek, J.R. Rostrup-Nilesen, J. Catal. 209 (2002) 365–384.
[47] H. Mori, C.-J. Wen, J. Otomo, K. Eguchi, H. Takahashi, Appl. Catal. A: Gen. 245 (2003) 79–85.
[48] Y. Li, X. Wang, C. Xie, C. Song, Appl. Catal. A: Gen. 357 (2009) 213–222.
[49] P.C. Das, N.C. Pradhan, A.K. Dalai, N.N. Bakhshi, Fuel Process. Technol. 85 (2004) 1487–1501.
[50] V. Modafferi, G. Panzera, V. Baglio, F. Frusteri, P.L. Antonucci, Appl. Catal. A: Gen. 334 (2008) 1–9.
[51] G. Italiano, C. Espro, F. Arena, F. Frusteri, A. Parmaliana, Appl. Catal. A: Gen. 357 (2009) 58–65.
[52] T.V. Reshetenko, L.B. Avdeeva, V.A. Ushakov, E.M. Moroza, A.N. Shmakov, V.V. Kriventsov, D.I. Kochubey, Yu.T. Pavlyukhin, A.L. Chuvilin, Z.R. Ismagilov, Appl. Catal. A: Gen. 270 (2004) 87–99.
[53] S. Takenaka, M. Ispida, M. Serizawa, E. Tanabe, K. Otsuka, J. Phys. Chem. B 108 (2004) 11464–11472.